Nano Research
DOI 10.1007/s12274-015-0891-y
Research Article
ISSN 1998-0124
CN 11-5974/O4

An ultra-sensitive dual-mode imaging system using metal-enhanced fluorescence in solid phantoms

Eran A. Barnoy[1], Dror Fixler[1] (✉), Rachela Popovtzer[1], Tsviya Nayhoz[1], and Krishanu Ray[2] (✉)

[1] *Faculty of Engineering and the Institute of Nanotechnology and Advanced Materials, Bar Ilan University, Ramat Gan 5290002, Israel*
[2] *Center for Fluorescence Spectroscopy, Department of Biochemistry and Molecular Biology, University of Maryland School of Medicine, Baltimore, MD 21201, USA*

Received: 15 June 2015
Revised: 26 August 2015
Accepted: 28 August 2015

KEYWORDS
gold nanoparticles, biomolecular imaging, noninvasive detection, diffusion reflection, fluorescence lifetime imaging, metal-enhanced fluorescence

ABSTRACT

In this study, we developed a highly sensitive dual-mode imaging system using gold nanoparticles (GNPs) conjugated to various fluorophores in solid phantoms. The system consists of fluorescence-lifetime imaging microscopy (FLIM) for surface imaging, diffusion reflection (DR) for deep-tissue imaging (up to 1 cm), and metal-enhanced fluorescence (MEF). We detected quenching in the fluorescent intensity (FI) for the conjugation of both gold nanospheres (GNS) and gold nanorods (GNRs) to Fluorescein, which has an excitation peak at a wavelength shorter than the surface plasmon resonance (SPR) of both types of GNPs. Enhanced FI was detected in conjugation to Rhodamine B (RhB) and Sulforhodamine B (SRB), both with excitation peaks in the SPR regions of the GNPs. The enhanced FI was detected both in solution and in solid phantoms by the FLIM measurements. DR measurements detected the presence of GNRs within the solid phantoms by recording the dropped rates of light scattering in wavelengths corresponding to the absorption spectra of the GNRs. With the inclusion of MEF, this promising dual-mode imaging technique enables efficient and sensitive molecular and functional imaging.

1 Introduction

Gold nanoparticles (GNPs) are promising theranostic agents relevant to bio-medicine, engineering, and chemistry [1–3] because they combine nontoxicity and biocompatibility [4, 5] with useful optical properties, including a large absorption cross-section [6] and tunable scattering characteristics [7]. Gold nanorods (GNRs) are especially interesting, with extreme absorption and scattering properties in the visible and near-infrared regions of the spectrum; these are enhanced by surface plasmon resonance (SPR) [8]. The absorption of GNRs can be tuned, by controlling the fabrication process, to the near-infrared window between 700 and 900 nm, a range that allows relatively high photon penetration into biological tissues.

Address correspondence to Dror Fixler, Dror.Fixler@biu.ac.il; Krishanu Ray, KRay@som.umaryland.edu

GNP-aided techniques have already been developed for X-ray imaging, computed tomography (CT), surface-enhanced Raman scattering, and photoacoustic tomography, including both *in vivo* and phantom experiments [9–12]. While X-ray and CT are useful for whole-body imaging at high resolutions, they have risks associated with exposure to ionizing radiation. Photoacoustic tomography uses safer wavelengths, but requires high-power laser intensities of ~15 mJ·cm^{-2}, which can thermally damage the surrounding tissues.

Multi-modal imaging can obtain more comprehensive pictures of a tissue than can be obtained from a single method. Our labs have previously reported a novel, inexpensive, and simple multi-modal imaging technique that can be used *in vivo*, which provides deep-volume imaging using diffusion reflection (DR) of tissues containing GNPs as contrast agents, and surface imaging through fluorescence-lifetime imaging microscopy (FLIM) [13].

DR spectroscopy is a simple, safe, and inexpensive optical diagnostic method. It can reveal morphological information on tissues using low-intensity radiation with low penetration depths [14–16]. In DR, the reflected light intensity profile of a tissue (I) is measured across a pre-specified range of light source-detector distances (ρ) [16, 17]. As discussed previously [18], the reflected intensity as a function of source-detector separation, $I(\rho)$, fits the following profile

$$I(\rho) = \frac{c_1}{\rho^2} e^{-\mu\rho} \quad (1)$$

where c_1 is a constant depending on the medium and the source and detector aperture sizes, and μ is the effective attenuation coefficient, which expresses both absorbance and scattering. Equation (1) can be rewritten as

$$\ln[\rho^2 I(\rho)] = c_2 - \mu\rho \quad (2)$$

where c_2 is $\ln(c_1)$. From Eq. (2), one sees that by measuring the expression $\ln(\rho^2 I(\rho))$ over several values of ρ, obtaining spectral information on the composition of the sample is simple, since the spectral properties are contained in μ as the slope of this function [17, 18]. GNPs as optical contrast agents can add specificity and sensitivity to DR with tunable absorption and scattering properties. In previous publications, we proved the high sensitivity of DR for tumor [18–20] and atherosclerosis [21] detection.

FLIM is an advanced spectroscopic tool that provides useful information in biological and biomedical applications [22, 23]. Traditional fluorescence imaging techniques are based on the fluorescence intensity (FI), measuring the total fluorescence signal of a sample, and have limited quantitative comparison abilities for molecular-level cellular function studies. While a stronger FI may indicate stronger activity in a specimen, it could also simply reflect a greater concentration of fluorescent molecules. In contrast, FLIM uses the fluorescence lifetime (FLT), which is a known quantity independent of molecule concentration for any fluorescent substance. FLIM can achieve spatial and temporal resolutions allowing intuitive quantitative analysis of the imaged regions [22, 23]. The image contrast in FLIM is based on the FLT at each pixel, rather than the total FI or fluorophore concentration, thus revealing information on the processes and intracellular structures that affect the FLT. When fluorophores are within 40 nm of GNPs, the FLT can be changed by the through-space interaction of the fluorophore and the GNP [24–27], making GNP-fluorophore constructs useful as FLIM targets.

Many studies have explored the capabilities of smart probes that could be activated to produce a signal only upon contact with a target of interest. Many researchers sought the detection of enzymatic activity [28–32], and many also developed efficient probes using GNPs [33–35]. Among the GNP-based probes that used fluorescence, the majority focused on the concept of quenching, in which proximity to the GNP reduced the FI; subsequent interaction with the target (e.g., cleavage of the connection by a restriction enzyme) would trigger normal fluorescent behavior [29, 36–38]. However, these techniques can be improved by the fluorescence-enhancing capabilities of metals, and of GNPs in particular. Because of the collective oscillation of surface electrons, or plasmons, metal particles of sub-wavelength size can experience enhancements in their local electric fields. The local fields can interact with nearby fluorophores, increasing rates of both excitation and radiative decay; by this mechanism, a higher quantum yield and improved photostability

can be obtained with less photobleaching as compared to those of fluorophores alone. When the excitation wavelength matches the absorption of both GNP and fluorophore, metal-enhanced fluorescence (MEF) is observed [24]. A fluorophore alone displays a FLT described by the following equation

$$\tau = \frac{1}{\Gamma + K_{nr}} \quad (3)$$

where τ is the FLT, Γ is the radiative decay rate, and K_{nr} is the non-radiative decay rate. The quantum yield (Q) of such a molecule is given by

$$Q = \frac{\Gamma}{\Gamma + K_{nr}} \quad (4)$$

Upon coupling to a metal particle, Eq. (3) for the FLT of the fluorophore becomes

$$\tau_m = \frac{1}{\Gamma + K_{nr} + \Gamma_m + K_m} \quad (5)$$

and Q, as in Eq. (4), becomes

$$Q_m = \frac{\Gamma + \Gamma_m}{\Gamma + K_{nr} + \Gamma_m + K_m} \quad (6)$$

where Γ_m and K_m are the new radiative and non-radiative decay rates that exist in the presence of the metal particle [24]. MEF has substantial implications; several studies have incorporated the MEF concept into smart probe designs [39–43]. We note two important factors: 1) The amount of MEF depends on the initial Q of the fluorophore, as Q cannot exceed 1 as shown in Eqs. (4) and (6); and 2) decreasing the distance between the fluorophore and the metal particle increases the possible enhancement, but this enhancement coincides with other local effects, most notably with resonance energy transfer, which leads to significant quenching close to the particle surface [22]. By choosing a particle of the correct size, fluorophore of the correct absorption peak, and linker of the correct length, efficient imaging probes can be created within tissues.

In this study, we fabricated dual-mode probes containing a nanometer-scale metal-to-dye spacer designed to reduce near-distance quenching and promote MEF. We performed DR and FLIM measurements with various GNP geometries including gold nanospheres (GNSs) and GNRs with two aspect ratios, each conjugated to one molecule of either Fluorescein (Flu) (absorption maximum ~470 nm, Q = 0.9), Rhodamine B (RhB) (absorption maximum ~554 nm, Q = 0.3), or Sulforhodamine B (SRB) (absorption maximum ~564 nm, Q = 0.8), the latter two of which exhibit excitation peaks in the GNP SPR, and so are better suited for both *in vivo* imaging and MEF. We measured the FLT of the probes in solution as well as in solid phantoms simulating biological tissues. While the dual-mode method previously demonstrated high sensitivity in phantoms, the method was based on quenching and sought areas of reduced fluorescence as targets. In this study, we demonstrated a highly sensitive dual-mode imaging system that uses enhanced, rather than quenched, FI in combination with FLT and DR.

2 Experimental

2.1 Nanoparticle fabrication and coating

For the purposes of this study we created three shapes of GNPs: GNSs and GNRs with two aspect ratios. The method of Enüstün and Turkevich was used to assemble GNSs with diameters of ~20 nm [44]. For this process, 414 μL of 50% $HAuCl_4$ was mixed into 200 mL distilled water and boiled. Upon boiling, 4.04 mL 10% sodium citrate was added, and the solution was stirred with heat for 5 min. The mixture was left to cool for about an hour. The nanoparticles were collected through repeated centrifugation.

The GNRs were constructed using a modified version of the Seed-Mediated Growth Method [45, 46]. Gold seeds were created by mixing 250 μL 0.01 M $HAuCl_4$ with 9.75 mL 0.1 M cetrimonium bromide (CTAB) and stirring. Then 600 μL 0.01 M $NaBH_4$ was added and the solution stirred for 10 min. After stirring, the mixture was allowed to sit for at least 1 h. In a flask, 95 mL 0.1 M CTAB was mixed with 5 mL 0.01 M $HAuCl_4$. To create shorter and longer nanorods, 0.6 and 1.2 mL 0.01 M silver nitrate was added, respectively. After, 550 μL of 0.1 M ascorbic acid was added, which turned the solution clear. From the previously created seed solution, 120 μL was added to the flask, and the solution was allowed to sit overnight. The following day, the particles were concentrated through centrifugation until a clear suspension was achieved.

All nanoparticles were coated with 15% polyethylene glycol (PEG)-NH_2 (M_W = 1,000 g·mol^{-1}, Creative PEGWorks, Winston Salem, USA) and 85% methoxy-PEG-SH (M_W = 1,000 g·mol^{-1}, Creative PEGWorks), by stirring the nanoparticles with the PEG particles for at least 3 h. Each type of particle was then divided into four groups. One group was left with only the PEG coating, while each of the other three was mixed with a different species of fluorophore, with a stoichiometric match between the fluorophore and PEG-NH_2. The three fluorophores used were Flu, RhB, and SRB (Sigma-Aldrich, Israel). In addition to these fluorophores, 1-ethyl-3-(3-dimethylaminopropyl) carbodiimide HCl (EDC) and N-hydroxysulfosuccinimide sodium salt (NHS) were added in similar concentrations as activating agents to aid the formation of bonds between the fluorophores and PEG chains by creating good leaving groups. The particles were stirred with the fluorophores overnight, and then centrifuged until clear suspensions were achieved. Dilutions were made of all particles; the final concentration of fluorophores in each sample was approximately 10 μM.

2.2 Solid phantom construction

Solid phantoms were created by mixing, by volume, 10% Intralipid (Lipofundin MCT/LCT 20%, B. Braun Melsungen AG, Germany) for scattering and 3% India ink (0.1%) for absorption, and 87% either distilled water, a nanoparticle solution, or a fluorophore solution. Agarose powder (SeaKem LE Agarose, Lonza, USA) was added at 1.2% to solidify the solution. The components were stirred with heating until even mixing was achieved; the mixture was then poured into wells. The wells were placed into a vacuum container to cool and solidify the mixture over a few hours.

A total of 27 phantoms were assembled. Three 4 mL phantoms were created as controls containing no GNP. One of these used distilled water only, one had 10 μM RhB, and the last had 5 μM RhB as the balance of the phantom solution mixture. The other 24 phantoms were all composed of a 400 μL inner phantom containing GNP and a 4 mL outer base phantom for contrast. With an outer base of water phantoms, a phantom was created for each particle type/fluorophore combination at two concentrations of 10 and 5 μM. This provided 18 water-based phantoms (3 particle types × 3 fluorophores × 2 concentrations = 18 phantoms). In addition, phantoms were created for each particle type bound to RhB at both 10 and 5 μM with a 10 or 5 μM RhB base (3 types of particles with RhB at 10 μM each + 3 types at 5 μM each = 6 phantoms with RhB base). The inner phantoms were created and solidified first as cylinders of ~5 mm diameter; these were placed in 15 mm wells, and the base phantom solutions were poured around them and allowed to solidify.

2.3 FLIM measurements: FI and FLT

Fluorescence measurements were obtained through a scanning confocal PicoQuant MicroTime 200 microscope (PQ MT200) with time-correlated single-photon counting abilities. The ps pulsed excitation laser (473 or 510 nm, repetition rate of 20 MHz, full width at half maximum (FWHM) of 80 ps) was reflected by a dichroic mirror into an inverted microscope (Olympus, IX71). A water-immersion objective (Olympus 60×, numerical aperture (NA) of 1.2) was used to focus the laser light onto the sample and to collect the FI emission from the sample. The FI signal passed through the dichroic mirror and band-pass filter was focused through a 75 μm pinhole to single-photon avalanche photodiode (SPAD, SPCM-AQR-14, Perkin Elmer Inc.) detectors. The samples containing Flu were excited by a 473 nm laser, using a 473/10 nm excitation laser clean-up filter, a Z476RDC dichroic filter, and a 520/40 collection bandpass filter (500–540 nm). The RhB and SRB samples were excited by a 510 nm laser, using a 510/10 nm excitation laser clean-up filter, a ZT514RDC dichroic filter, and a 550 long-pass collection filter. FLIM images, including both FLT and FI information, were recorded by raster-scanning the samples through the excitation light, focused by a linearized piezo scanner. All analyses were performed using PQ Symphotime software.

2.4 DR measurements

DR measurements were conducted on the same phantoms used for FLIM, using a device designed for noninvasive optical imaging (NEGOH-OP TECHNOLOGIES, Israel), as previously described [18, 19]. Two laser diodes of wavelengths of 650 and 780 nm served as excitation sources; a 125 μm diameter

optical fiber was used for irradiation. A photodiode was placed in contact with the surface of the phantom to detect scattered light while minimizing ambient light and potential losses at the edges. The light source was moved on a micrometer-scale plate in steps of 250 μm, allowing the light intensity reaching the photodiode to be measured at varying distances ρ between the source and detector. The initial and final separations were ~1 and ~5–6 mm, respectively. The reflected light intensity at the photodiode, $I(\rho)$, was measured using a digital scope (Agilent Technologies, Mso7034a, Santa Clara, CA, USA), and data was processed using LabView software.

3 Results and discussion

3.1 GNP fabrication

For the purposes of this work, we fabricated and measured three types of GNPs: GNSs and GNRs with two aspect ratios. The GNSs had diameters of 20 nm, and the GNRs were either 12 nm × 30 nm (GNR690) or 12 nm × 40 nm (GNR760). Each particle type was bound to Flu, RhB, and SRB separately. The separation distance between the fluorophores and GNPs was controlled using a PEG linker with M_W = 1 kDa, estimated as 10 nm in length. Figure 1 depicts schematics of the preparation and conjugation of the particles. Figure 2(a) displays the normalized absorption spectrum of each GNP alone, as well as each fluorophore alone, while Figs. 2(b)–2(d) show transmission electron microscope (TEM) images of the GNSs and GNRs produced by these processes. From the spectra, the absorption peak of RhB and SRB are notably very close to, but larger than, the absorption peak corresponding to the SPR associated with the short side of the GNRs, while the absorption peak of Flu is at a shorter wavelength than this SPR peak.

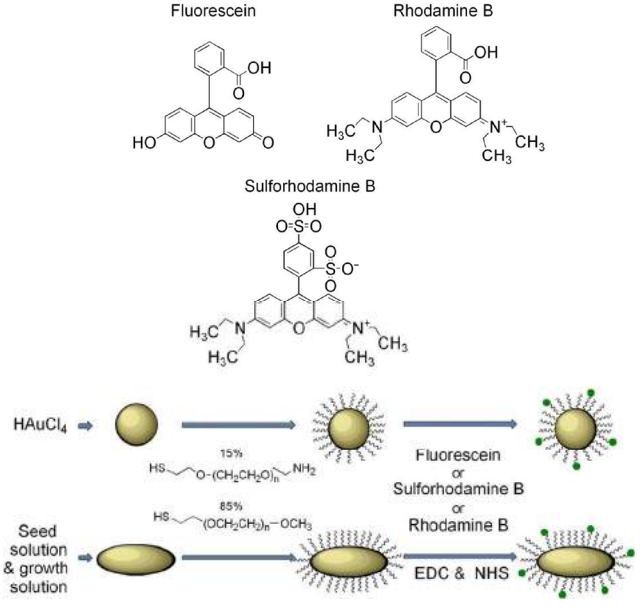

Figure 1 Schematic of preparation and subsequent conjugation of GNSs and GNRs to fluorophores.

3.2 Fluorescence measurement of solutions

FLIM was used to image the GNP-fluorophore constructs, as described in section 2.3. Figure 3 presents the FI measurements taken from the solutions of each GNP-fluorophore construct after dilution to total fluorophore concentrations of 1 μM. The FI measurements of each unbound fluorophore are presented at the same concentration for reference purposes.

The effects of conjugating GNPs to the fluorophores are visible in Fig. 3. For both RhB and SRB, which have absorption peaks in the SPR range of the GNPs, GNP conjugation allows increased FI compared to that of the unbound fluorophores, regardless of the GNP geometry. Thus, the image demonstrates MEF by the enhanced fluorescence signals following GNP

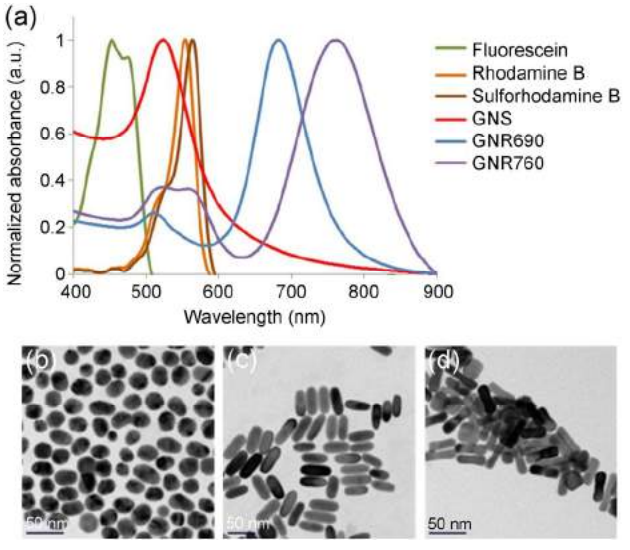

Figure 2 Particle characteristics. (a) Normalized absorption spectra of GNS, GNR690, GNR760, Fluorescein, Rhodamine B, and Sulforhodamine B; TEM images of synthesized (b) GNS, (c) GNR690, and (d) GNR760.

conjugation. The absorption peak for Flu lies below the SPR, and we observe reduced FI, or quenching, for all three GNP geometries.

3.3 FLIM measurement of solid phantoms

To image the localization of fluorescent constructs in samples, phantoms containing the conjugated GNP-fluorophores were imaged by scanning confocal FLIM. Figures 4(a) and 4(b)–4(d) display the FLT curves detected from the solid phantoms containing RhB alone and GNPs-RhB constructs, respectively, while Figs. 4(e)–4(f) depict representative FLT histograms of GNR690-RhB and GNR780-RhB. Figures 5(a) and 5(c) present FLIM images of solid phantoms containing RhB alone (a) and (c), while Figs. 5(b) and 5(d)–5(f) depict those of the GNP-RhB constructs. In Figs. 5(a) and 5(b), the FLIM images are shown as FI only, while Figs. 5(c)–5(f) show a combination of FI as brightness and FLT as color. The consistent green color indicates similar FLTs measured in all four phantoms. The increased apparent brightness indicates that the conjugation of RhB with any of the three GNPs greatly

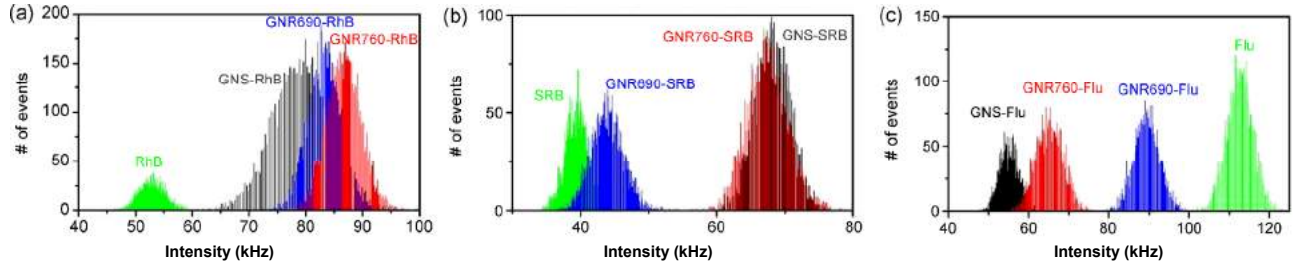

Figure 3 FI enhancement and quenching due to GNP conjugation in solution. FI is depicted in photon counts per millisecond, or kilohertz. (a) Count rate histograms of GNS, GNR690, and GNR760 conjugated to RhB. FI of RhB solution without GNPs is also included in the panel for comparison. (b) Count rate histograms of GNS, GNR690, and GNR760 conjugated to SRB. FI of SRB is included in the panel for comparison. (c) Count rate histograms of GNS, GNR690, and GNR760 conjugated to Flu. FI of Flu is included in the panel for comparison. All solutions contained a fluorophore concentration of 1 μM. All measurements for a given fluorophore are obtained under identical conditions, set-up, and excitation power.

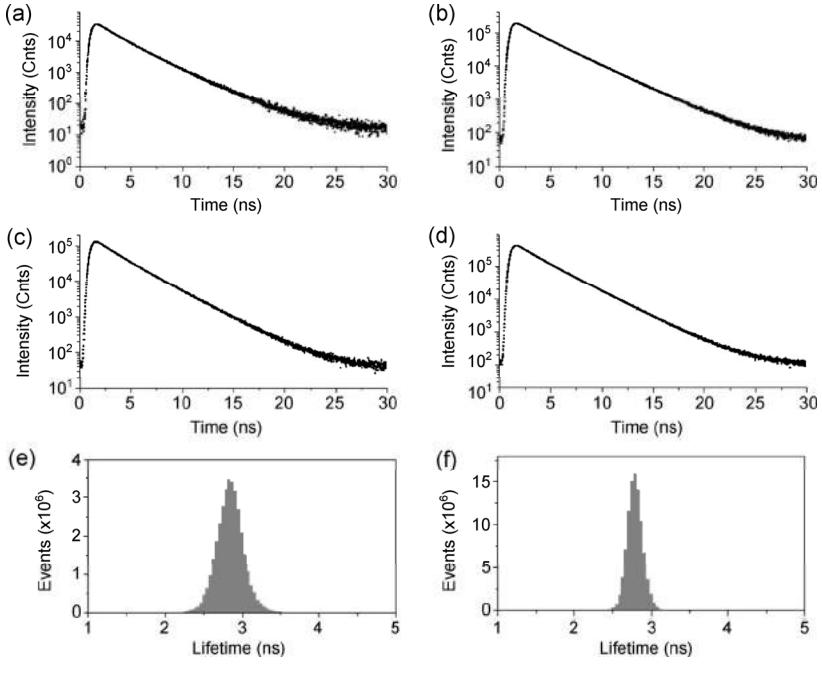

Figure 4 Representative FLT curves obtained from FLIM for RhB-based phantoms containing (a) RhB only, (b) GNS-RhB, (c) GNR690-RhB, and (d) GNR780-RhB. Representative FLT histograms for the same phantoms containing (e) GNR690-RhB and (f) GNR780-RhB. All curves are obtained under identical conditions, set-up, and excitation power.

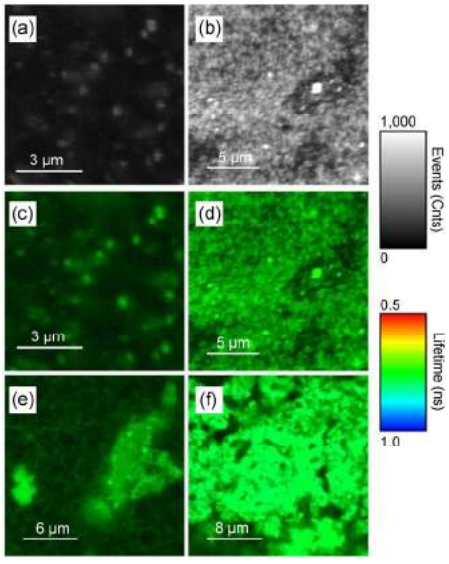

Figure 5 FLIM images of RhB-based phantoms. Depicting only FI (shown in counts of fluorescence events), the images show phantoms containing (a) RhB only and (b) GNS-RhB. Combining FI (shown as brightness) and FLT (shown as color), the images show phantoms containing (c) RhB only, (d) GNS-RhB, (e) GNR690-RhB, and (f) GNR760-RhB. For all images, the gray (brightness) scale bar represents FI in counts per millisecond. The color scale bar displays the FLT range in ns. All images are obtained under identical conditions, set-up, and excitation power.

increases the detectable FI in a phantom environment. With MEF, a sample can be imaged and GNP-fluorophore conjugations can be detected by locating the bright areas. Figure 6 shows the FLIM images for SRB and Flu conjugated to each of the three GNPs types. As in Fig. 5, the images are shown as a combination of FI brightness and FLT color. Figure 6 demonstrates the potential to accurately image regions containing the constructs, as the localization of the constructs in the phantoms creates bright spots in FLIM imaging.

3.4 DR measurements of solid phantoms

DR was used to detect GNP presence in the same solid phantoms measured through FLIM, following the procedure described in section 2.4. By measuring the intensity of reflected light from the phantom, denoted as $I(\rho)$, over varying separation distances ρ between the light source and detector, the slope of $\ln(\rho^2 I(\rho))$ versus ρ was calculated for the phantoms containing only water, GNS, and each type of GNR. As explained in section 1, Eq. (2), the slope of this line

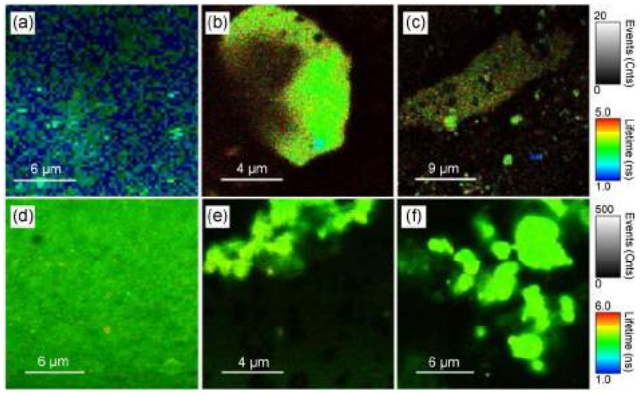

Figure 6 FLIM images of phantoms containing (a) GNS-SRB, (b) GNR690-SRB, (c) GNR760-SRB, (d) GNS-Flu, (e) GNR690-Flu, and (f) GNR760-Flu. Each gray scale bar applies to all images in the row, and represents FI in counts per ms. Each color scale bar applies to all images in the row, and displays the FLT range in ns. All images for a given fluorophore are obtained under identical conditions, set-up, and excitation power.

directly describes the spectral properties (absorbance and scattering) of the sample, or in this case the phantom. Figure 7 shows the results for each type of phantoms using a 780 nm light source. In these DR plots, more pronounced slopes indicate greater degrees of particle absorption. As expected, Fig. 7 shows that

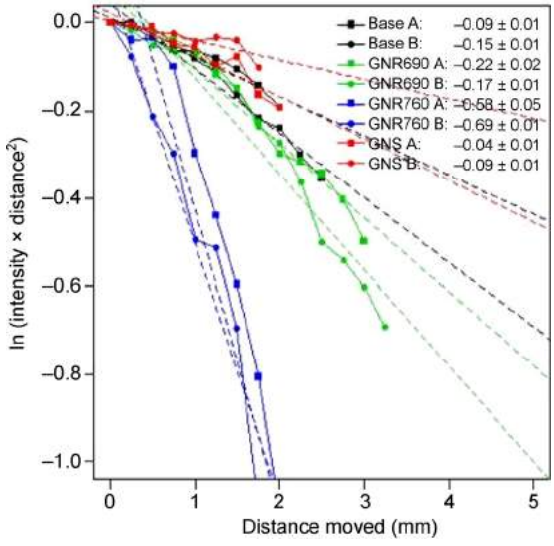

Figure 7 DR measurements of scattered light intensity as a function of distance from four phantoms: water-only (black), GNR690 (green), GNR760 (blue), and GNS (red). Each phantom was measured twice, as denoted by the marker shapes. The light source had a wavelength of 780 nm, and the phantoms were designed to contain 5 μM fluorophore. The legend shows the slope ± standard error to the slope of a line fitted to the corresponding curve. Equation (2) explains that this slope indicates the spectral properties of the sample.

the longer GNRs with a peak at 760 nm absorb the source light most efficiently, while the shorter GNRs are less efficient. Meanwhile, the GNS and water phantoms perform similarly, because of the very low absorption of GNSs at 780 nm (see Fig. 2(a)). Since none of the tested fluorophores absorb this wavelength, the DR system only differentiates between the different GNPs geometries. For this reason, only four phantoms are presented in Fig. 7: One has no GNPs, one has GNS, one has GNR690, and one has GNR760, where each GNP is conjugated to RhB. By tuning the wavelength of the probing light used by the DR system, we can efficiently test for the presence of corresponding particles within a sample volume.

4 Conclusions

In this study, we demonstrated that FLIM and DR measurements can sensitively detect the presence of GNPs in tissue-like phantoms. The technique makes use of MEF through the proper choice of fluorophore species and controlling the separation distance between the fluorophores and the GNPs. We achieved MEF with two different fluorophores with different excitation peaks at wavelengths longer than the SPR wavelength of the GNPs. Furthermore, we witnessed MEF both in solution and in solid phantoms. This implies that we may create efficient optical GNP-based probes spanning multiple excitation wavelengths. However, the degree of enhancement depends on the original quantum yield of the imaged fluorophore, meaning that a fluorophore with bright intrinsic fluorescence would not be greatly affected by GNP conjugation. Despite the sensitivity of the imaging, FLIM provided only surface fluorescence information. Meanwhile, DR provided a degree of deep-tissue imaging, revealing the presence of GNPs within phantoms by detecting changes in the optical properties of the tissue phantom.

With efficient GNP-fluorophore constructs, we produced enhanced-fluorescence images with FLIM and then detected the presence of GNPs with DR in the same phantoms. Through the use of phantoms, we gained insight into the behavior of tissues in similar imaging situations. Both detection methods are non-invasive, simple, and highly sensitive; combining them with MEF produced a very promising imaging tool for medical diagnostic procedures.

Acknowledgements

This work was partially supported by the U.S. National Institutes of Health (Nos. AI087968 and NIGMS R01GM117836 (K.R.)). The authors thank Dr. J. Lakowicz for access to the FLIM facility at the Center for Fluorescence Spectroscopy.

References

[1] Cao, Y. C.; Jin, R. C.; Mirkin, C. A. Nanoparticles with Raman spectroscopic fingerprints for DNA and RNA detection. *Science* **2002**, *297*, 1536–1540.

[2] Rosi, N. L.; Mirkin, C. A. Nanostructures in biodiagnostics. *Chem. Rev.* **2005**, *105*, 1547–1562.

[3] Nie, S. M.; Xing, Y.; Kim, G. J.; Simons, J. W. Nanotechnology applications in cancer. *Annu. Rev. Biomed. Eng.* **2007**, *9*, 257–288.

[4] Eghtedari, M.; Liopo, A. V.; Copland, J. A.; Oraevsky, A. A.; Motamedi, M. Engineering of hetero-functional gold nanorods for the *in vivo* molecular targeting of breast cancer cells. *Nano Lett.* **2009**, *9*, 287–291.

[5] Von Maltzahn, G.; Park, J. H.; Agrawal, A.; Bandaru, N. K.; Das, S. K.; Sailor, M. J.; Bhatia, S. N. Computationally guided photothermal tumor therapy using long-circulating gold nanorod antennas. *Cancer Res.* **2009**, *69*, 3892–3900.

[6] El-Sayed, M. A. Some interesting properties of metals confined in time and nanometer space of different shapes. *Acc. Chem. Res.* **2001**, *34*, 257–264.

[7] Jain, P. K.; Lee, K. S.; El-Sayed, I. H.; El-Sayed, M. A. Calculated absorption and scattering properties of gold nanoparticles of different size, shape, and composition: Applications in biological imaging and biomedicine. *J. Phys. Chem. B* **2006**, *110*, 7238–7248.

[8] Zhang, Y. N.; Yu, J.; Birch, D. J. S.; Chen, Y. Gold nanorods for fluorescence lifetime imaging in biology. *J. Biomed. Opt.* **2010**, *15*, 020504.

[9] Copland, J. A.; Eghtedari, M.; Popov, V. L.; Kotov, N.; Mamedova, N.; Motamedi, M.; Oraevsky, A. A. Bioconjugated gold nanoparticles as a molecular based contrast agent: Implications for imaging of deep tumors using optoacoustic tomography. *Mol. Imaging Biol.* **2004**, *6*, 341–349.

[10] Qian, X.; Peng, X.-H.; Ansari, D. O.; Yin-Goen, Q.; Chen, G. Z.; Shin, D. M.; Yang, L.; Young, A. N.; Wang, M. D.; Nie, S. *In vivo* tumor targeting and spectroscopic detection with surface-enhanced Raman nanoparticle tags. *Nat. Biotechnol.* **2008**, *26*, 83–90.

[11] Robinson, J. T.; Welsher, K.; Tabakman, S. M.; Sherlock, S. P.; Wang, H. L.; Luong, R.; Dai, H. J. High performance *in vivo* near-IR (>1 μm) imaging and photothermal cancer therapy with carbon nanotubes. *Nano Res.* **2010**, *3*, 779–793.

[12] Reuveni, T.; Motiei, M.; Romman, Z.; Popovtzer, A.; Popovtzer, R. Targeted gold nanoparticles enable molecular CT imaging of cancer: An *in vivo* study. *Int. J. Nanomedicine* **2011**, *6*, 2859–2864.

[13] Fixler, D.; Nayhoz, T.; Ray, K. Diffusion reflection and fluorescence lifetime imaging microscopy study of fluorophore-conjugated gold nanoparticles or nanorods in solid phantoms. *ACS Photonics* **2014**, *1*, 900–905.

[14] Subhash, N.; Mallia, J. R.; Thomas, S. S.; Mathews, A.; Sebastian, P.; Madhavan, J. Oral cancer detection using diffuse reflectance spectral ratio R540/R575 of oxygenated hemoglobin bands. *J. Biomed. Opt.* **2006**, *11*, 014018.

[15] McMurdy, J.; Jay, G.; Suner, S.; Crawford, G. Photonics-based *in vivo* total hemoglobin monitoring and clinical relevance. *J. Biophotonics* **2009**, *2*, 277–287.

[16] Ankri, R.; Taitelbaum, H.; Fixler, D. Reflected light intensity profile of two-layer tissues: Phantom experiments. *J. Biomed. Opt.* **2011**, *16*, 085001.

[17] Ankri, R.; Taitelbaum, H.; Fixler, D. On phantom experiment of the photon migration model in tissues. *Open Opt. J.* **2011**, *5*, 28–32.

[18] Ankri, R.; Duadi, H.; Motiei, M.; Fixler, D. *In-vivo* tumor detection using diffusion reflection measurements of targeted gold nanorods—Aquantitative study. *J. Biophotonics* **2012**, *5*, 263–273.

[19] Ankri, R.; Peretz, V.; Motiei, M.; Popovtzer, R.; Fixler, D. A new method for cancer detection based on diffusion reflection measurements of targeted gold nanorods. *Int. J. Nanomedicine* **2012**, *7*, 449–455.

[20] Fixler, D.; Ankri, R. Subcutaneous gold nanorods [corrected] detection with diffusion reflection measurement. *J. Biomed. Opt.* **2013**, *18*, 61226.

[21] Ankri, R.; Leshem-Lev, D.; Fixler, D.; Popovtzer, R.; Motiei, M.; Kornowski, R.; Hochhauser, E.; Lev, E. I. Gold nanorods as absorption contrast agents for the noninvasive detection of arterial vascular disorders based on diffusion reflection measurements. *Nano Lett.* **2014**, *14*, 2681–2687.

[22] Lakowicz, J. R. *Principles of Fluorescence Spectroscopy*, 3rd ed.; Springer: New York, NY, 2006.

[23] Becker, W. Fluorescence lifetime imaging—Techniques and applications. *J. Microsc.* **2012**, *247*, 119–136.

[24] Lakowicz, J. R. Radiative decay engineering 5: Metal-enhanced fluorescence and plasmon emission. *Anal. Biochem.* **2005**, *337*, 171–194.

[25] Ray, K.; Szmacinski, H.; Enderlein, J.; Lakowicz, J. R. Distance dependence of surface plasmon-coupled emission observed using Langmuir-Blodgett films. *Appl. Phys. Lett.* **2007**, *90*, 251116.

[26] Ray, K.; Badugu, R.; Lakowicz, J. R. Polyelectrolyte layer-by-layer assembly to control the distance between fluorophores and plasmonic nanostructures. *Chem. Mater.* **2007**, *19*, 5902–5909.

[27] Ray, K.; Zhang, J.; Lakowicz, J. R. Fluorescence lifetime correlation spectroscopic study of fluorophore-labeled silver nanoparticles. *Anal. Chem.* **2008**, *80*, 7313–7318.

[28] Kobayashi, H.; Choyke, P. L. Target-cancer-cell-specific activatable fluorescence imaging probes: Rational design and *in vivo* applications. *Acc. Chem. Res.* **2011**, *44*, 83–90.

[29] Drake, C. R.; Miller, D. C.; Jones, E. F. Activatable optical probes for the detection of enzymes. *Curr. Org. Synth.* **2011**, *8*, 498–520.

[30] Li, X. H.; Gao, X. H.; Shi, W.; Ma, H. M. Design strategies for water-soluble small molecular chromogenic and fluorogenic probes. *Chem. Rev.* **2014**, *114*, 590–659.

[31] Lavis, L. D.; Raines, R. T. Bright building blocks for chemical biology. *ACS Chem. Biol.* **2014**, *9*, 855–866.

[32] Prost, M.; Hasserodt, J. "Double gating"—A concept for enzyme-responsive imaging probes aiming at high tissue specificity. *Chem. Commun.* **2014**, *50*, 14896–14899.

[33] Razgulin, A.; Ma, N.; Rao, J. H. Strategies for *in vivo* imaging of enzyme activity: An overview and recent advances. *Chem. Soc. Rev.* **2011**, *40*, 4186–4216.

[34] Hutter, E.; Maysinger, D. Gold-nanoparticle-based biosensors for detection of enzyme activity. *Trends Pharmacol. Sci.* **2013**, *34*, 497–507.

[35] Zhang, J. M.; Li, C.; Zhang, X.; Huo, S. D.; Jin, S. B.; An, F. F.; Wang, X. D.; Xue, X. D.; Okeke, C. I.; Duan, G. Y. et al. *In vivo* tumor-targeted dual-modal fluorescence/CT imaging using a nanoprobe co-loaded with an aggregation-induced emission dye and gold nanoparticles. *Biomaterials* **2015**, *42*, 103–111.

[36] Cheng, W.; Chen, Y. L.; Yan, F.; Ding, L.; Ding, S. J.; Ju, H. X.; Yin, Y. B. Ultrasensitive scanometric strategy for detection of matrix metalloproteinases using a histidine tagged peptide-Au nanoparticle probe. *Chem. Commun.* **2011**, *47*, 2877–2879.

[37] Park, S. Y.; Lee, S. M.; Kim, G. B.; Kim, Y. P. Gold nanoparticle-based fluorescence quenching via metal coordination for assaying protease activity. *Gold Bull.* **2012**, *45*, 213–219.

[38] Tira, D. S.; Focsan, M.; Ulinici, S.; Maniu, D.; Astilean, S. Rhodamine B-coated gold nanoparticles as effective "turn-on"

fluorescent sensors for detection of zinc II ions in water. *Spectrosc. Lett.* **2014**, *47*, 153–159.

[39] Mohamed, M. B.; Volkov, V.; Link, S.; El-Sayed, M. A. The "lightning" gold nanorods: Fluorescence enhancement of over a million compared to the gold metal. *Chem. Phys. Lett.* **2000**, *317*, 517–523.

[40] Geddes, C. D.; Lakowicz, J. R. Editorial: Metal-enhanced fluorescence. *J. Fluoresc.* **2002**, *12*, 121–129.

[41] Ming, T.; Zhao, L.; Yang, Z.; Chen, H. J.; Sun, L. D.; Wang, J. F.; Yan, C. H. Strong polarization dependence of plasmon-enhanced fluorescence on single gold nanorods. *Nano Lett.* **2009**, *9*, 3896–3903.

[42] Abadeer, N. S.; Brennan, M. R.; Wilson, W. L.; Murphy, C. J. Distance and plasmon wavelength dependent fluorescence of molecules bound to silica-coated gold nanorods. *ACS Nano* **2014**, *8*, 8392–8406.

[43] Kang, K. A.; Wang, J. T. Smart dual-mode fluorescent gold nanoparticle agents. *Wiley Interdiscip. Rev.: Nanomed. Nanobiotechnol.* **2014**, *6*, 398–409.

[44] Enüstün, B. V.; Turkevich, J. Coagulation of colloidal gold. *J. Am. Chem. Soc.* **1963**, *85*, 3317–3328.

[45] Nikoobakht, B.; El-Sayed, M. A. Preparation and growth mechanism of gold nanorods (NRs) using seed-mediated growth method. *Chem. Mater.* **2003**, *15*, 1957–1962.

[46] Sau, T. K.; Murphy, C. J. Seeded high yield synthesis of short Au nanorods in aqueous solution. *Langmuir* **2004**, *20*, 6414–6420.